ELSEVIER

Novel electrochemical and thermodynamic conditioning approaches and their evaluation for open cathode PEM-FC stacks

F. Becker [a,*,1], C. Cosse [b,1], C. Gentner [a], D. Schulz [b], L. Liphardt [c]

[a] German Aerospace Center (DLR), Institute of Engineering Thermodynamics, Hein-Saß-Weg 22, 21129 Hamburg, Germany
[b] Helmut-Schmidt-University - University of the Federal Armed Forces Hamburg, Holstenhofweg 85, 22043 Hamburg, Germany
[c] Airbus Operations GmbH, Kreetslag 10, 21129 Hamburg, Germany

HIGHLIGHTS

- PtOx formation and membrane dry out can be prevented by a minimum current, to produce enough water and avoid OCV.
- A start up after soaking the stack in water showed severe flooding issues but afterwards an improvement is seen.
- The reconditioning procedure provided by air starvation of 100 s helps to provide 6,2% more el. energy.
- Post-processing algorithm filters noisy EIS data and thus improves the stationary accuracy of the resulting model.

ARTICLE INFO

ABSTRACT

The Air-cooled and open cathode proton exchange fuel cell (PEMFC) offers particular advantages in terms of complexity and weight reduction. Therefore, it seems very attractive to support the aviation industry in their de-carbonisation process. Major challenges in terms of operational stability and reliability hinders this technology to be used in commercial applications.

Therefore, this study thoroughly examines the conditioning and optimization of open cathode PEMFC stacks, drawing insights from experimental findings. Key areas of focus include the enduring impact of pre-humidification, the quantification of efficiency enhancements through reconditioning via oxygen starvation, and the refinement of Electrochemical Impedance Spectroscopy (EIS) data analysis under non-stationary conditions.

The pre-humidification enhances stack performance by improving cell voltages from 40.09 V to 41.37 V at 30 A, increasing membrane humidity and improving efficiency. Furthermore, the residual water in the stack also functions as evaporative cooling and can assist in limiting the operating temperature of the stack during system start up. However, it is demonstrated that excessive soaking with water leads to severe flooding phenomena at the beginning of operation.

A reconditioning period of 100 s through oxygen starvation induces a notable increase in stack voltage, from 41.37 V to 47.79 V at 35 A, which decreases to 43.56 V after 10 min of operation. This corresponds to an average increase in electric energy provision of about 6.2% at constant hydrogen consumption, attributed to PtOx reduction and increased water production.

Despite limitations outside the medium frequency range (approximately 10 Hz – 15 kHz) for non-stationary conditions, EIS aids in understanding of the stack behaviour and supports the interpretation of current and voltage results. A novel evaluation method enables the quantitative description of the condition using EIS data. This data reveals a considerable drop (on average about 21,5% for the 10 A point and about 27,4% for the 30 A point) in charge transfer resistances of the fuel cell from initial operation to measurements after overnight soaking and the first series of oxygen starvation recovery.

1. Introduction

The operation of a fuel cell is a complex process that combines the electrochemical reaction with mass transport, energy conversion, momentum and charge transport [1,2]. The PEMFC is supplied with hydrogen on the anode side and oxygen from the air on the cathode side. The reaction products are water, electrical and thermal energy. Products and reactants are transported in and out of the fuel cell via channels in the bipolar plate [3]. The generated heat is mainly transported via the coolant through the coolant channels in the bipolar plates. The used coolant can be liquid or gaseous. Water or water-glycol mixtures are generally used as the liquid medium and ambient air is generally used as the gaseous medium. The air-cooled and open cathode PEMFC offers particular advantages in terms of complexity and weight when the cooling and cathode channels are combined, in comparison to conventional liquid-cooled PEMFCs and seems therefore very attractive to support the aviation industry in their de-carbonisation process [4].

To accelerate the de-carbonisation, it is necessary to fulfil the requirements for high power densities while maintaining high efficiency and durability. A simple way to improve toward the performance goals is to operate the fuel cell at its maximum allowable temperature. An increased operating temperature leads to an improved power output due to faster reaction kinetics and decreasing ohmic losses in the membrane, thus increasing the performance [5–7]. On the other hand, the operating temperature affects the maximum theoretical voltage at which a fuel cell can operate. A higher temperature corresponds to a lower theoretical maximum voltage and lower theoretical efficiency. In addition, the temperature also has a major influence on the water management of the fuel cell. The ionic conductivity of the membrane, a crucial factor for the efficiency of the fuel cell, is mainly influenced by its humidity. Consequently, the temperature indirectly affects the efficiency and possible performance of the fuel cell by facilitating increased water absorption at elevated temperatures [8–11].

Many studies are available on analytical and numerical modelling [12–25] of PEMFCs and several researchers have concentrated on the area of thermal modelling as well as thermal and water management [26–39] Chupin et al. presented in [29] a one-dimensional model and Yu and Jung [32] developed a two-dimensional numerical thermal model of a water-cooled PEMFC. Yu's and Jung's heat transfer sub-model included the conductive heat transfer inside the MEA and convective heat rejection from MEA to cooling water flow and gases. In [40] Ondrejička et al. explore the limits of using air cooling for PEMFC stacks. They presented a numerical thermal model in order to analyse the heat transfer and predict the temperature distribution in air-cooled PEMFCs.

Studies on open cathode stacks are primarily concerned with operational stability under varying environmental and operational conditions, as well as active and passive measures to improve it [41–49]. Yu et al. describe in [41,42] the sensibility of the stack performance when the anode end cell performs as the weakest cell. To mitigate this sensibility, they described the use of endplate heaters [41] and copper endplates with carbon paper [42], which leads to a more uniform temperatures and stress distribution.

Another barrier is the susceptibility to contaminants due to the open design of an air-cooled open cathode fuel cell system. Contaminants very often cause reversible performance losses and can be removed by special operation strategies. For example, specific cell potentials, such as low cathode potentials and high anode potentials, can be applied to recover from contamination-related degradation mechanisms [11]. Furthermore, test procedures have been developed to evaluate the effect of reversible and irreversible performance degradation on the fuel cell behaviour during operation [50–52]. In [51] Gazdzicki et al. used defined test blocks under specific load cycles and recovery phases to recover the reversible performance loss and separate that effect from irreversible losses. In [53] Zago et al. analysed and described a performance loss mechanism due to PtOx formation. Several studies demonstrated that an operation under low potentials, caused by H_2/N_2

conditioning or high currents, causes a PtOx reduction [54–57]. Balogun et al. demonstrated in [57], that cathode starvation leads to an accelerated conditioning procedure for PEMFCs. In comparison to protocols proposed by the US Department of Energy (DOE) and European Union (EU) and to an amperometric conditioning protocol, this protocol reached the target power 10 times faster and with a lower degradation rate during cycling experiments.

The aim of this study is to clarify whether used and degraded air-cooled open cathode stacks are irreversibly or reversibly degraded and to demonstrate that stacks, previously thought irreversibly damaged can be recovered by special procedures.

2. Experimental

The scientific issues to be clarified with the help of experimental investigations of this work can be divided into three main topics.

2.1. Pre-humidification of the stack

The maximum performance of a fuel cell stack is strongly influenced by the ohmic losses that occur in the membranes. These in turn can be influenced during operation by internal and external humidification. Soaking the stack in water the day before the experiments, is expected to reduce the ohmic resistance to a minimum. The effect of this method on the operatinoal behaviour of the stack is determined.

2.2. Reconditioning of the stack by air starvation

In order to minimise reversible efficiency losses caused by PtOx formation, the stack is operated under air starving conditions ($\lambda \ll 1$). An oxide-free platinum surface is expected to achieve better performance results. The performance gain and duration to recover the PtOx formation are quantified.

2.3. EIS - Measurements for non-stationary conditions

To assess the impact of the mentioned conditioning methods on the electrochemical processes within the fuel cell stack, a series of Electrochemical Impedance Spectroscopy (EIS)-measurements is conducted. Given the challenges associated with maintaining a consistent stationary operation to get reliable results from the EIS-measurements, a novel method is presented, which enables automated identification and targeted exclusion of unreliable data points from the subsequent analysis. This allows meaningful analysis of EIS data obtained under nonideal conditions in a short time frame.

2.4. Experimental setup

For the experimental investigations, an AC64 – Open-Cathode-Stack from *Intelligent Energy* with a gross power output of 2 kW, consisting of 72 single cells, each with a nominal electrode area of ~60 cm^2, was used. The metallic bipolar plates with a thickness of 0.1 mm have a straight flow field design on the cathode. The structure of the open cathode consists of alternating channels for cathode and cooling channels. The schematic drawing of the experimental setup is depicted in Fig. 1.

The gas supply of pressurized hydrogen is regulated by a manual pressure regulator valve (PRV) at the inlet of the anode side of the stack, which is set to 700 mbar relative to the environment. It should be noted that 700 mbar corresponds to the maximum fuel supply pressure according to the datasheet [58]. To recirculate unused hydrogen and humidity to the stack, a 24 V diaphragm pump is used. Another benefit of using this pump is a more homogeneous media and temperature distribution at the anode side in comparison to a setup without such a pump. As diffused nitrogen and water from the cathode side needs to be released, a purge valve is implemented at the anode exhaust line of the
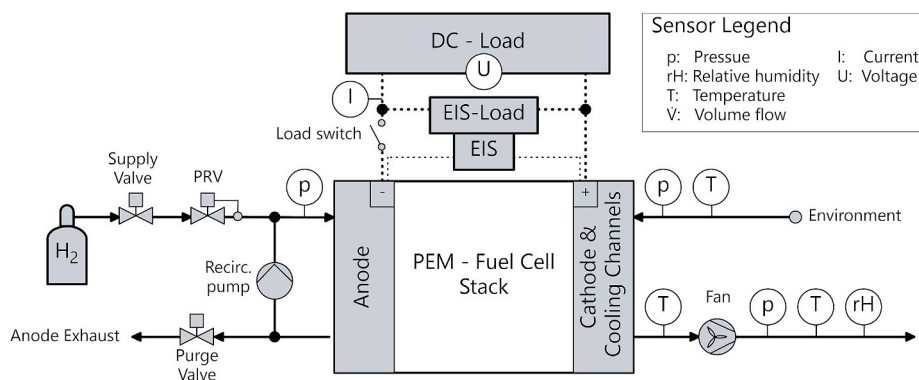
Fig. 1. A schematic description of the test setup is shown. The test station has a hydrogen and air supply, with the air supplied being used for reaction and cooling. The current is regulated via an electric DC-load, if necessary, a potentiostat can also be switched on for EIS-measurements.

stack and opens every 30 s. To avoid pressure surges on the Membrane Electrode Assemblies (MEAs), due to the comparatively large pressure difference of the anode system to the environment, the purge valve is controlled by Pulse Width Modulation (PWM). This allows a moderate rate of pressure increase and decrease during the purge process compared to a solenoid valve, which is often used for liquid-cooled stacks.

The cathodic air supply and cooling are realized with an axial fan (*San Ace 120*) located at the cathode outlet of the stack. Environmental air is sucked through the stack, thereby a more even flow and temperature distribution across the stack can be achieved.

The speed of the fan is set proportional to the required volume flow rate. Since the volume flow of air required for cooling the stack is higher than the volume flow required for oxygen supply, a measurement of the exhaust gas temperature is used to control the fan speed. The temperatures of the cathode are measured at the cathode in- and outlet of the stack. For the experimental test regarding pre-humidification, an additional IR-camera (FLIR A655SC) was used.

To control the electric power output of the stack, a thermal DC-load (*H&H PLI 6412*) is used, which allows potentiostatic and galvanostatic operation of the stack. Additionally, a frequency response analyser is used, which is further described in Section 2.4.

2.5. Pre-humidification of the stack

After system start up, the stack is operated for 30 min at a current of 10 A and afterwards at 30 A without previous knowledge about the state of the stack. During this start up procedure, three EIS-measurements are carried out at each of the two current levels. Subsequently, the load is released to 3 A and held for 3 min, followed by load steps of 10 A, 20 A, 30 A and 40 A for the same duration. After a reconditioning procedure according to Section 2.3, the same load steps were measured again in ascending and descending order to obtain a VI-Curve as reference. After the system shut-down, the stack is removed from the test-rig. Pre-humidification of the stack is achieved by pouring approximately 1 l of demineralized water evenly to the cathode of the stack. The stack is then placed in a sealed container for at least 12 h. The pre-humidified stack is placed in the test bench again and an IR-Camera is measuring the temperature distribution of the cathode inlet during system start up. During start up, the current is stepwise increased up to 35 A.

2.6. Reconditioning by oxygen starvation

To recover reversible voltage losses due to PtOx formation at the cathodic catalyst layer, first the system is started and a current of 5 A is set, avoiding OCV. Then, the cathode fan is switched off, which will result in a voltage drop due to oxygen starvation. 5 s after the stack voltage reaches 0 V, the current is set to 0 A to stop the oxygen

consumption of the stack. As soon as OCV is reached again, the procedure is repeated two times more. Subsequently, the fan is started again to bring the stack back into operation. To determine the influence of this procedure, it is performed directly after system start and after operation for an extended period under load in a second experiment.

2.7. Electrochemical impedance spectroscopy - measurements

In order to identify the effect of the mentioned recovery methods on the electrochemical processes within the fuel cell stack, a number of EIS-measurements are performed. A Zahner IM6 system is used in conjunction with the H&H electric load. The Zahner system is used to add a DC current of 1 A and an AC modulation of 96 mA in sinusoidal form. The investigated frequency ranges from 50 kHz down to 250 mHz, comparable to EIS-measurements on PEMFC in other publications [59–61]. Using this setup, the first measurements at a current of 10 A and 30 A for the dry and non-conditioned state were performed. The second series of EIS-measurements includes current steps of 3 A, 10 A, 20 A and 30 A after humidification and reconditioning of the stack.

At the upper end of the frequency spectrum the data is expected to exhibit poor quality, due to unavoidable parasitic influences of the measurement setup, at the lower frequency end, the data is expected to become unreliable, due to the non-stationary operation of the open cathode stack. As the anode supplies using regular purging, as well as the system cooling, featuring a rather simplistic control algorithm, the system is unable to reach a truly stationary operating state.

The measured data will be analysed using a modified version of the PyEIS python toolbox. The first step is the linear Kramers-Kronig test proposed by Boukamp et al. [62], which is implemented with an automated selection of the required number of RC-elements proposed by Schönleber et al. [63]. The measured impedance is fitted with an ohmic resistor (R_{ohm}) and N RC-elements in Voigt configuration, resulting in the following equation giving the impedance (Z):

$$Z = R_{ohm} + \sum_{k=2}^{N} \frac{R_k}{1 + j\omega\tau_k}. \tag{1}$$

R_k is the real resistance of the kth RC element and τ_k the respective relaxation time. The relative residuals are defined in [62] as:

$$\Delta Z^{'} = \frac{Z^{'} - Z^{'}(\omega)}{|Z(\omega)|}, \Delta Z^{''} = \frac{Z^{''} - Z^{''}(\omega)}{|Z(\omega)|} \tag{2}$$

For a more detailed description of the process the reader is referred to [62,63]. While the relative residuals can indicate questionable data, they are not suitable as a judging criterion to exclude bad data points from the further analysis, since the model used to calculate the relative residuals might be heavily influenced by the respective data. An ideal impedance spectrum will not contain drastic changes in magnitude and phase of the impedance over the frequency range. Therefore, a new

algorithm is proposed to evaluate the measurement data and eliminate excessively noisy data using four judging variables:

$$\Delta Z_i = \left| \frac{\left| \frac{|Z_{i-1}| - |Z_{i+1}|}{2} - |Z_i| \right|}{|Z_i|} \right| > \Delta_{\text{cont}}, \Delta\phi_i = \left| \frac{\left| \frac{|\phi_{i-1}| - |\phi_{i+1}|}{2} - |\phi_i| \right|}{|\phi_i|} \right| > \Delta_{\text{cont}} \quad (3)$$

$$\Delta\phi_{ii0} = \left| 1 - \left| \frac{\phi_{i0}}{\phi_i} \right| \right| > \Delta_{\text{grad}}, \Delta\phi_{ii1} = \left| 1 - \left| \frac{\phi_{i1}}{\phi_i} \right| \right| > \Delta_{\text{grad}}. \quad (4)$$

Going through the measured data points, i, at all frequencies the algorithm checks whether any of the conditions in Eqs. (3) and (4) are true. In the event one or more of the conditions are true, the data point for that respective frequency is disregarded for the following analysis. Furthermore, the data points with the highest and lowest frequency will be disregarded, since there is no data with a higher or lower frequency to compare them to, to evaluate Eq. (3). Eq. (3) ensures, that the spectrum is sufficiently continuous, while eq. (4) prevents excessive gradients, which are also not expected. The parameters will need to be adapted, in order to find a trade-off between the accuracy of the data and the limitation of the range of investigation.

3. Results

3.1. Stack operation

The electric parameters of the stack as well as the in- and outlet temperature and outlet humidity during the initial measurement of the dry and non-conditioned state of the stack are depicted in Fig. 2. The two load steps, each with three conducted EIS-measurements are indicated. The added DC current of 1 A during the measurement with the AC modulation of 96 mA by the EIS load is not displayed in the figure. Thus, the actual current and power during the EIS-measurements were slightly higher. However, the measured voltage accurately indicates the stack response to the total DC current and AC modulation. Therefore, the voltage dips indicate when the EIS-measurements took place.

After system start up, the outlet temperature of the stack increases due to dissipation of the thermal reaction power. In addition, a slight increase in the humidity of the cathode outlet can be observed. After increasing the current from 10 A to 30 A, a further increase in temperature and humidity can be seen. However, the measured humidity subsequently continues to decrease so that a steady state condition is not present even after 30 min of operation. During this period, a continuous increase in the recorded stack voltage was observed, starting at 40.11 V just before the first EIS-measurement at 30 A, reaching 40.47 V 130 s after the third EIS-measurement.

The subsequent load reduction immediately leads to a decrease in the exhaust gas temperature and humidity. Additionally, the subsequent step-wise current increase reveals the proportional relation between the amount of product water and heat generated to the current and the outlet humidity of the stack.

The reconditioning procedure according to Section 2.3 was performed two times afterwards. The corresponding measurement results are shown in Fig. 3.

The OCV displays a gradual increase after the first three phases of
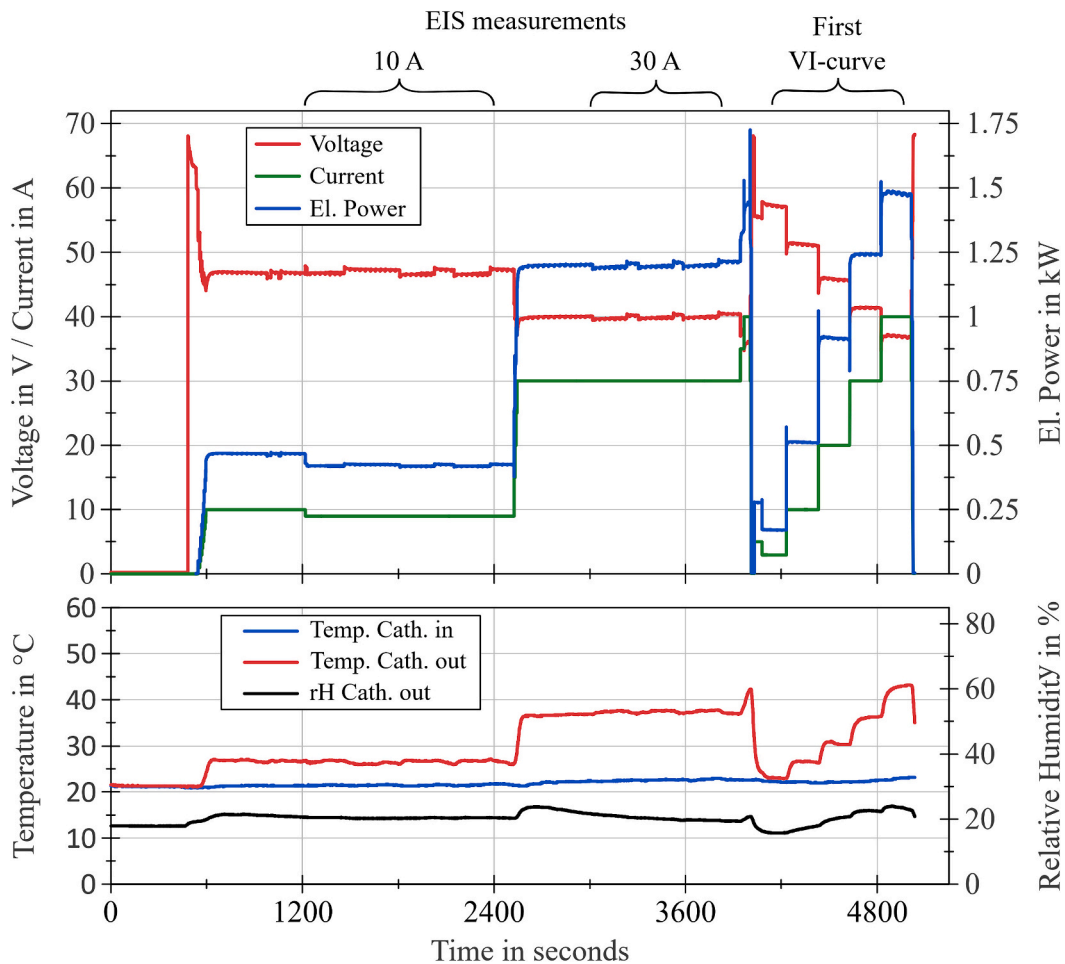

Fig. 2. Relevant operating parameter of fuel cell stack during initial operation of dry and non-conditioned stack including impedance measurements at 10 and 30 A and a subsequent recording of a VI-curve.
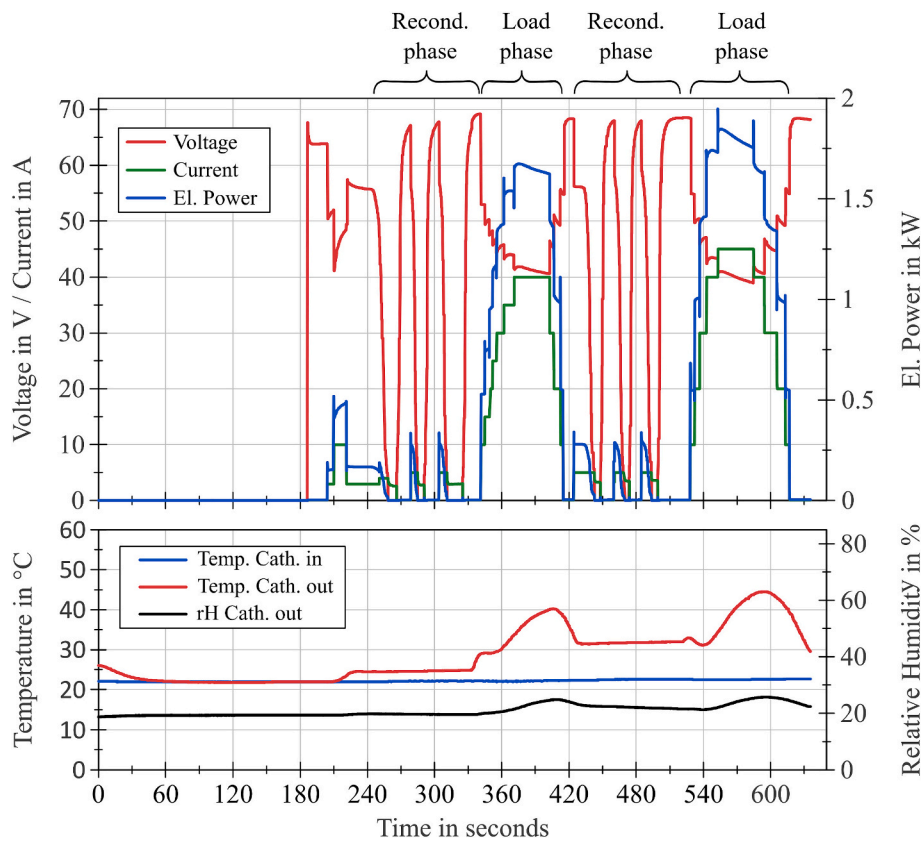
Fig. 3. Relevant operating parameter of fuel cell stack during two reconditioning phases of the stack by oxygen starvation, each followed by operation under load.
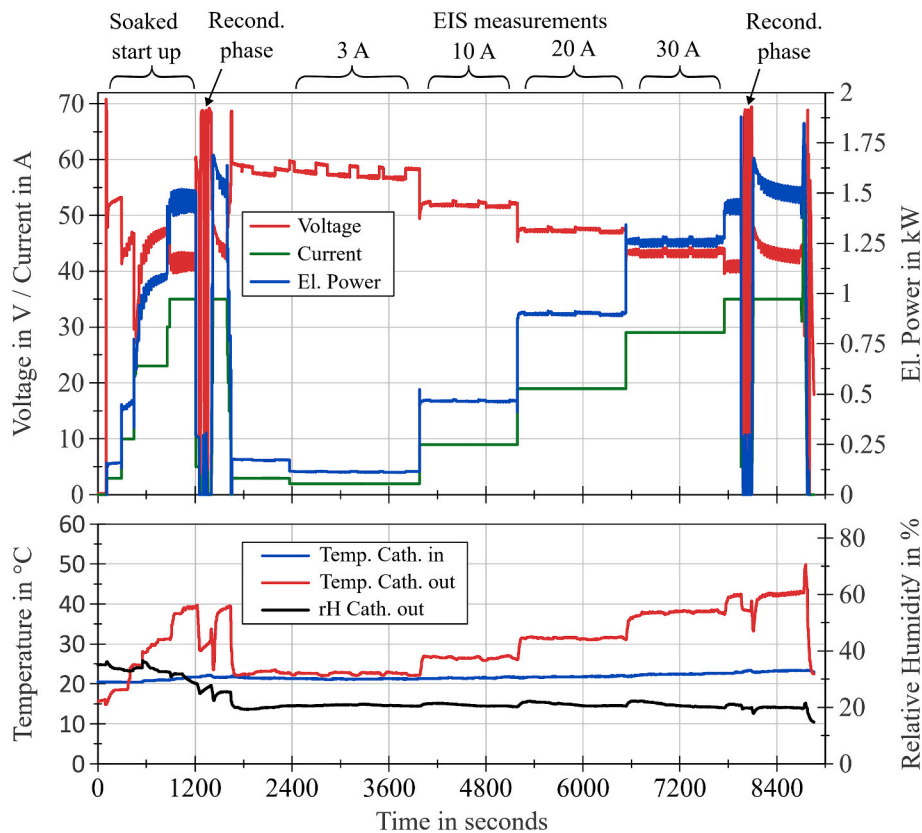

Fig. 4. Relevant operating parameter of pre-humidified fuel cell stack after overnight soaking including two reconditioning phases prior to and after the impedance measurement series at 3, 10, 20 and 30 A.

starvation: 67.13 V, 67.37 V, and 69.15 V. Subsequent to the first reconditioning phase, the current was increased to 40 A. Here a maximum voltage of 41.82 V was achieved. Then, the stack voltages continuously decreased, while the temperature and humidity at the cathode outlet of the stack continuously increased. The repetition of the reconditioning phase resulted in a maximum voltage peak of 43.52 V at 40 A. The subsequent increase in current to 45 A resulted in a maximum voltage of 41.03 V, which dropped continuously to 39.09 V during the holding period of 30 s.

It has to be mentioned, that the measured outlet temperature of the stack during the reconditioning phases cannot be trusted as the cathode fan was shut off during this time. Consequently, no forced convection of the cathode gas took place.

After this measurement, a second VI-curve was obtained, with each data point corresponding to a current step held for 180 s, serving as reference points for the further analysis.

The measurement results of the pre-humidified stack after overnight soaking are depicted in Fig. 4. Compared to the previous measurements, a higher OCV of 70.81 V was initially achieved. However, the following increase in current led to significant voltage drops, which recovered only gradually and exceeded those observed under typical operation conditions.

The observed phenomenon wherein the outlet temperature results in a lower value compared to the inlet temperature of the stack at the beginning of system operation can be attributed to the evaporation enthalpy of the additional water in the stack due to pre-humidification. However, this effect is not sustainable. After 280 s of operation, the outlet temperature was equal to the inlet temperature. During this time, an electrical energy of 17.7 Wh was provided by the stack.

At a current of 35 A an increased cell voltage fluctuation can be observed. This is related to the anode-side purge, whose influence on the cell voltage increases with higher current density and correspondingly higher hydrogen consumption changing the anode pressure. The average stack voltage before the first reconditioning phase of the measurement equals 43.20 V. Afterwards, a peak stack voltage of 48.23 V was measured, which continuously decreased to 44.05 V after 172 s.

In Fig. 4 the EIS-measurements at the different load steps are indicated as well. The measured relative humidity at the cathode outlet stays constant in this time except for marginal changes during the load changes. Furthermore, a continuous decrease of cell voltage occurs especially at the first current step of 3 A.

Before the final reconditioning phase of the measurement a stack voltage of 41.85 V was measured at 35 A. After the reconditioning phase, 47.79 V was achieved, which continuously decreased to 43.56 V after 600 s.

3.2. EIS measurements

Using a modifiedPyEIS Python toolbox [64], the measurement data has been plotted and analysed. As can be seen in Fig. 4, the EIS measurements at 3 A were all conducted under non-stationary conditions, as evidenced by the drop of the voltage from the first to the last measurement. These measurements will, therefore, be used to test different values for Δ_{cont} and Δ_{grad}. The relative Kramers-Kronig residuals for the third EIS measurement at 3 A are shown in Fig. 5 (further points in Appendix A 1) for the raw data and three combinations of parameters for Δ_{cont} and Δ_{grad} (5/12.5; 10/25; 20/50%). The relative residuals (Eq. 2) of the measurements result from a fit with Eq. (1) using the process described in [62,63].

In Fig. 5, the magnitude of the residuals indicates unreliable data, which does not conform to the Kramers-Kronig relations. This was expected, as discussed above, so now in the further process, special care needs to be taken in order to ensure only valid conclusions are drawn from the data. Comparing Fig. 5 (a) and (b) shows a significant reduction of the residuals with any of the proposed parameters, however, the best results are achieved using the combination 10/25%, which will be used in the following further analysis. Fig. 6 shows the Nyquist plot of the processed data of all measurements at 3 A, Fig. 6 (b) in particular visualises the high frequency region, where the membrane resistance is the dominating.

Eventhough the data in Fig. 6 (b) does not show the actual crossing of the impedance spectrum with the real axis of the Nyquist plot, it clearly shows how the data tends toward a new impedance value with every subsequent measurement after the recovery procedures.

Fig. 7 (a) shows a Nyquist plot of the raw measurement data over the entire frequency range for the impedance measurements at 10 A prior to the overnight soaking. Fig. 7 (b) shows the Bode plot of both impedance magnitude $|Z|$ and phase angel ϕ over the entire measured range and Fig. 7 (d) and (e) show the respective data for the measurements on the next day after the soaking. Especially in this second set of plots a lot of instability can be observed, especially for the high and low frequency regions of the measured data. Comparing Fig. 7 (a) and (d), already shows the reduced impedance of the stack due to the recovery procedure. Fig. 7 (e) and (f) show the relative residuals (Eq. 2) of the first measurements resulting from a fit with Eq. (1) using the process described in [62,63]. In both cases, the magnitude of the residuals indicates bad data, which does not conform to the Kramers-Kronig relations and is therefore not reliable. This was expected, as discussed above, so now in the further process, special care needs to be taken in order to ensure only valid conclusions are drawn from the data.

Fig. 8 visualises the effect the proposed algorithm has on the quality of the subsequently performed fit. All experimental data sets are fitted
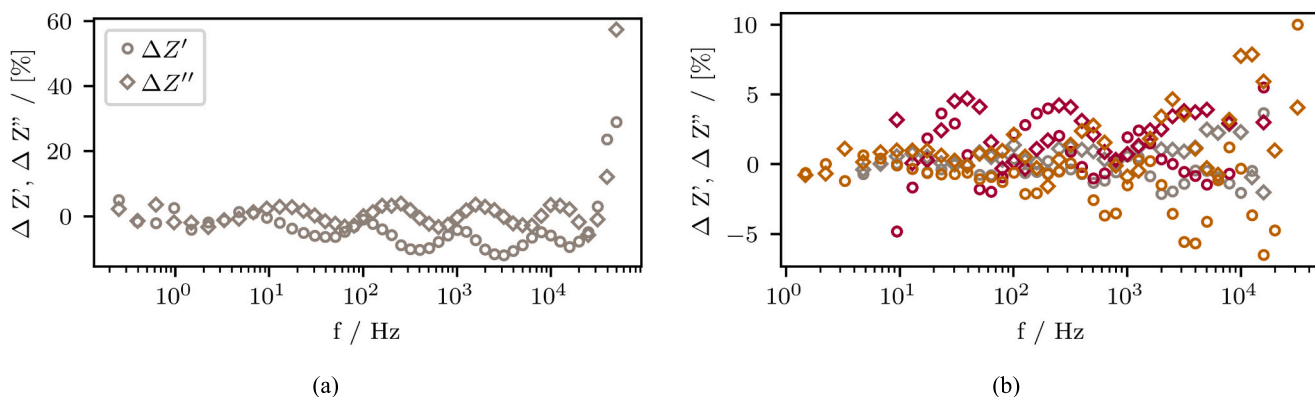
Fig. 5. (a) Residuals of the real part, $\Delta Z'$ (○), and the imaginary part, $\Delta Z''$ (◇), from the linear Kramers-Kronig test of the raw data at 3 A current after the overnight soaking of the stack; (b) Kramers-Kronig residuals of the processed data using 5/12.5% (red), 10/25% (grey) and 20/50% (yellow) for $\Delta_{cont}/\Delta_{grad}$. (For interpretation of the references to colour in this figure legend, the reader is referred to the web version of this article.)
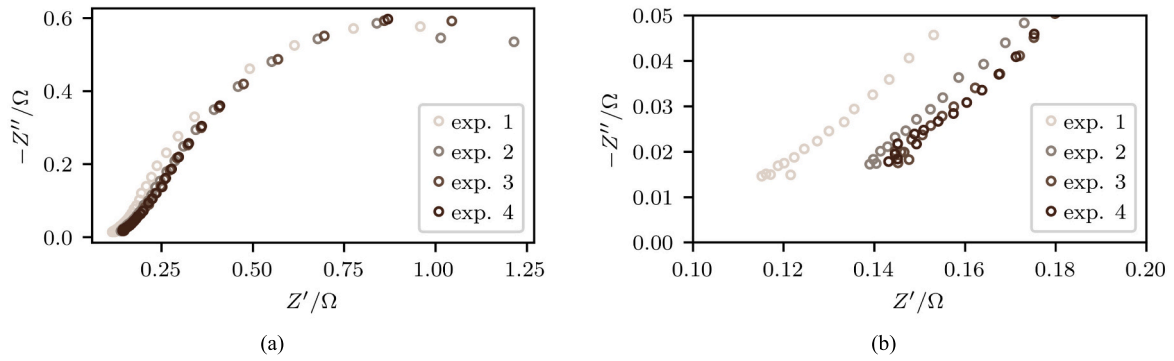
Fig. 6. (a) Nyquist plot of the processed data of all four EIS measurements at 3 A, (b) high frequency part of the Nyquist plot.
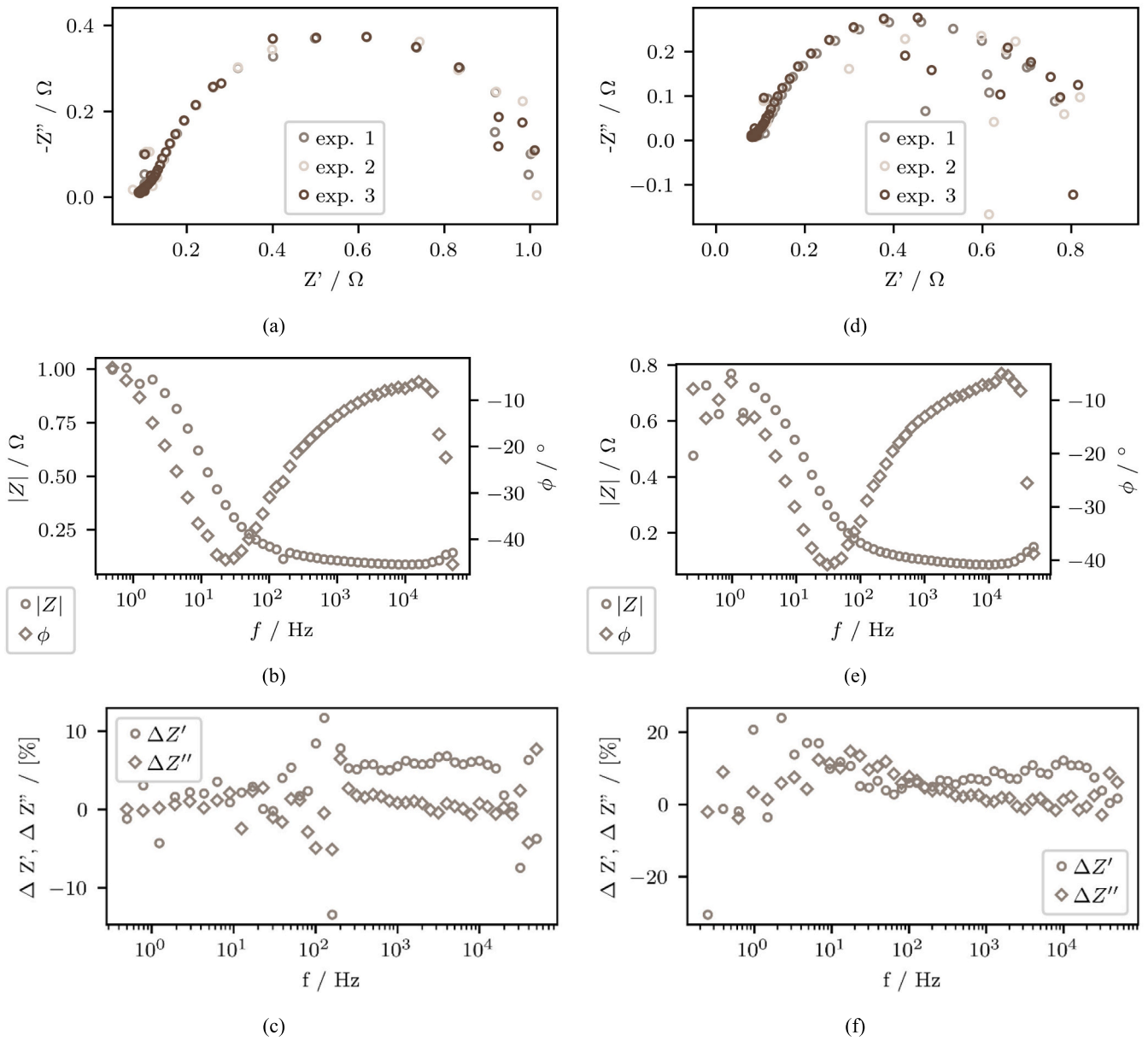
**Fig. 7.** (a) Nyquist plot of the raw experimental data, (b) Bode plot of magnitude, |Z| (○), and phase angle. Φ (◇) from exp. 1 and (c) residuals of the real part, $\Delta Z'$ (○), and the imaginary part, $\Delta Z'$ (◇), from the linear Kramers-Kronig test data for 10 A current prior to the overnight soaking of the stack; (d), (e) and (f) show the respective plots after overnight soaking.

Fig. 8. Bode plot of the measured and processed data as well as the respective fits, highlighted data points were excluded from the optimised fits, solid lines represent the magnitude, $|Z|$, and dotted the phase angle, Φ. (a) measurement at 10 A and (b) at 30 A prior to overnight soaking, (c) 10 A and (d) 30 A after the soaking.
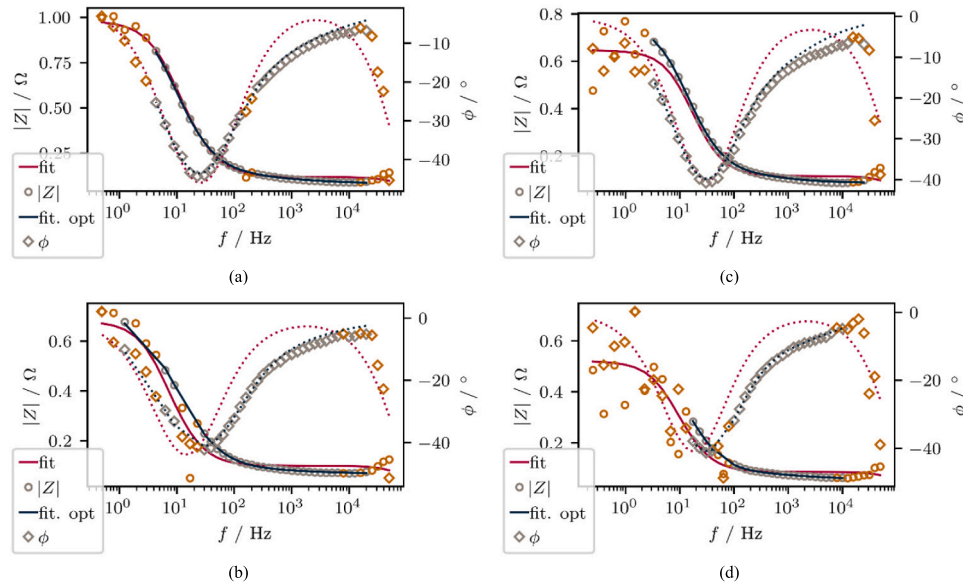
with a complex nonlinear least square (CNLS) algorithm to estimate the optimal parameters for a Voigt configuration R-RQ-RQ equivalent circuit. In Fig. 8 noisy data points, which were identified through the criteria given in Eqs. (3) and (4) are highlighted. Then the original fit using all measured data points and the optimised fit, without the highlighted measurements are displayed in the Bode plots for the previously discussed measurements (further plots in Appendix A 1).

It is both visually, from Fig. 8, and numerically, from Table 1, apparent, that the quality of the fit is improved through the elimination of excessively noisy data from the source data. In most cases the fit is improved by four orders of magnitude, the minimal improvement is for three orders of magnitude, which is still quite significant. R_1 and R_2 represent the ohmic losses, which can be associated with the different processes in the electrodes of the fuel cell. The larger of the two, R_1,

decreases on average by 21.5 and 11.7% at 10 and 30 A respectively, due to the reconditioning procedures. For the smaller resistance R_2, the reduction at 10 A is even more significant, with 50.7% (average), however, at 30 A, this parameter is actually increased by 36.1% (average). Further, the value of R_1 at 10 A increases with each measurement after the overnight soaking (Table 1), a similar trend can be seen for the previous measurements at 3 A (Table A2.1).

Apart from the improvement of the fitting, the algorithm also identifies the data points, which represent reliable measurements and, therefore, allow analysis of the stacks performance. The minimum of the stacks impedance in the frequency range between 500 Hz and 10 kHz is more or less equal to the membrane resistance, which is the fitting parameter R_s. Table 2 presents the absolute and relative changes of the membrane resistance in the measurement and fitting due to the

Table 1
Values of the fitted parameters of the equivalent circuit calculated with a complex nonlinear least square algorithm and the calculated χ^2-value as a measure of the goodness of the respective fit.

Fit	R_s [Ω]	R_1 [Ω]	Q_1 [F s$^{n_1-1}$]	n_1	R_2 [Ω]	Q_2 [F s$^{n_2-1}$]	n_2	χ^2
10 A (1) dry	1.18×10^{-2}	8.61×10^{-1}	3.10×10^{-2}	9.19×10^{-1}	1.05×10^{-1}	2.12×10^{-5}	1.00×10^{0}	1.32×10^{-3}
10 A (1) dry opt.	7.86×10^{-2}	8.81×10^{-1}	3.92×10^{-2}	8.85×10^{-1}	6.06×10^{-2}	2.90×10^{-1}	5.00×10^{-1}	2.24×10^{-7}
10 A (1) wet	1.54×10^{-2}	5.33×10^{-1}	3.20×10^{-2}	9.37×10^{-1}	9.82×10^{-2}	2.01×10^{-5}	1.00×10^{0}	5.65×10^{-3}
10 A (1) wet opt.	8.50×10^{-2}	6.50×10^{-1}	4.11×10^{-2}	8.72×10^{-1}	3.65×10^{-2}	1.84×10^{-1}	5.99×10^{-1}	2.40×10^{-6}
10 A (2) dry	1.21×10^{-2}	8.71×10^{-1}	3.16×10^{-2}	9.43×10^{-1}	1.06×10^{-1}	1.94×10^{-5}	1.00×10^{0}	2.59×10^{-3}
10 A (2) dry opt.	7.95×10^{-2}	9.24×10^{-1}	4.06×10^{-2}	8.73×10^{-1}	5.25×10^{-2}	2.73×10^{-1}	5.04×10^{-1}	2.06×10^{-7}
10 A (2) wet	2.21×10^{-2}	6.25×10^{-1}	4.87×10^{-2}	8.73×10^{-1}	8.60×10^{-2}	2.44×10^{-5}	1.00×10^{0}	5.53×10^{-3}
10 A (2) wet opt.	8.05×10^{-2}	6.67×10^{-1}	3.79×10^{-2}	8.93×10^{-1}	4.01×10^{-2}	2.03×10^{-1}	5.97×10^{-1}	1.65×10^{-6}
10 A (3) dry	1.00×10^{-2}	8.86×10^{-1}	3.68×10^{-2}	8.93×10^{-1}	1.06×10^{-1}	2.09×10^{-5}	1.00×10^{0}	1.12×10^{-3}
10 A (3) dry opt.	8.04×10^{-2}	8.67×10^{-1}	3.35×10^{-2}	9.18×10^{-1}	6.21×10^{-2}	3.01×10^{-1}	5.00×10^{-1}	1.01×10^{-6}
10 A (3) wet	1.08×10^{-2}	6.64×10^{-1}	5.54×10^{-2}	8.27×10^{-1}	9.66×10^{-2}	2.17×10^{-5}	1.00×10^{0}	2.87×10^{-3}
10 A (3) wet opt.	7.98×10^{-2}	7.81×10^{-1}	5.88×10^{-2}	7.90×10^{-1}	9.81×10^{-3}	4.53×10^{-3}	1.00×10^{0}	4.63×10^{-6}
30 A (1) dry	1.09×10^{-2}	5.82×10^{-1}	6.58×10^{-2}	9.35×10^{-1}	8.78×10^{-2}	2.59×10^{-5}	1.00×10^{0}	1.54×10^{-2}
30 A (1) dry opt.	6.54×10^{-2}	6.40×10^{-1}	6.84×10^{-2}	8.26×10^{-1}	1.84×10^{-2}	5.14×10^{-1}	5.00×10^{-1}	4.03×10^{-7}
30 A (1) wet	1.01×10^{-2}	4.36×10^{-1}	7.18×10^{-2}	9.20×10^{-1}	7.47×10^{-2}	2.52×10^{-5}	1.00×10^{0}	3.12×10^{-2}
30 A (1) wet opt.	6.00×10^{-2}	5.10×10^{-1}	6.63×10^{-2}	8.40×10^{-1}	1.26×10^{-2}	5.94×10^{-3}	1.00×10^{0}	1.05×10^{-8}
30 A (2) dry	2.28×10^{-2}	6.22×10^{-1}	8.17×10^{-2}	9.04×10^{-1}	7.84×10^{-2}	2.96×10^{-5}	1.00×10^{0}	3.22×10^{-2}
30 A (2) dry opt.	6.29×10^{-2}	6.41×10^{-1}	6.56×10^{-2}	8.33×10^{-1}	2.06×10^{-2}	2.44×10^{-1}	5.49×10^{-1}	1.16×10^{-7}
30 A (2) wet	2.34×10^{-2}	4.77×10^{-1}	1.10×10^{-1}	8.68×10^{-1}	6.24×10^{-2}	3.58×10^{-5}	1.00×10^{0}	3.86×10^{-2}
30 A (2) wet opt.	5.31×10^{-2}	4.16×10^{-1}	4.35×10^{-2}	9.36×10^{-1}	4.23×10^{-2}	3.67×10^{-1}	5.00×10^{-1}	4.92×10^{-9}
30 A (3) dry	1.99×10^{-2}	5.90×10^{-1}	3.89×10^{-2}	9.99×10^{-1}	7.75×10^{-2}	2.85×10^{-5}	1.00×10^{0}	8.50×10^{-3}
30 A (3) dry opt.	6.48×10^{-2}	6.80×10^{-1}	7.26×10^{-2}	8.07×10^{-1}	1.34×10^{-2}	6.01×10^{-2}	7.10×10^{-1}	1.62×10^{-7}
30 A (3) wet	7.51×10^{-2}	3.19×10^{-1}	2.30×10^{-1}	1.00×10^{0}	1.70×10^{-1}	3.64×10^{-2}	1.00×10^{0}	3.85×10^{-2}
30 A (3) wet opt.	5.73×10^{-2}	4.96×10^{-1}	6.52×10^{-2}	8.43×10^{-1}	1.65×10^{-2}	3.52×10^{-2}	7.51×10^{-1}	1.15×10^{-7}

Table 2

Averaged measurement and fitting values for the membrane resistance at two different operating points before and after the overnight soaking and the relative differences between these values.

	processed measurements			optimised fitting		
	dry	wet	rel. diff.	dry	wet	rel. diff.
10 A	$8.70 \times 10^{-2}\,\Omega$	$8.17 \times 10^{-2}\,\Omega$	−6.16%	$7.95 \times 10^{-2}\,\Omega$	$8.18 \times 10^{-2}\,\Omega$	2.90%
30 A	$6.85 \times 10^{-2}\,\Omega$	$6.20 \times 10^{-2}\,\Omega$	−9.53%	$6.43 \times 10^{-2}\,\Omega$	$5.68 \times 10^{-2}\,\Omega$	−11.7%
rel. Diff.	−21.3%	−24.1%		−19.0%	−30.5%	

reconditioning procedures and the operating current. The data shows, that an increased current has a more pronounced effect on the membrane resistance, than the overnight soaking of the stack. This behaviour can be observed in the measurement data, as well as in the fitting results. Furthermore, the measured ohmic resistance of the stack decreases at the 10 A operating point after the performed procedures (−6.16%), whereas the respective fitting parameter increases slightly (+2.90%). The values for the goodness of the fitting (χ^2) of the measurements at 10 A before the soaking show a slightly better fitting result, than after the soaking (comp. Table 1).

4. Discussion

The experimental results already showed parametric relationships and potential for improvement regarding the conditioning of Open-Cathode-PEM-FC-Stacks. Main topics for the analysis and discussion can be summarised as follows:

- The external pre-humidification influences the membrane hydration and the stack cooling.
- O_2-starvation reduces the PtOx amount on the cathode catalyst layer.
- The improvement of data validity by the proposed algorithm for the the analysis of the EIS-measurement data obtained under non-stationary conditions

4.1. Pre-humidification of the stack

In order to identify the influence of pre-humidification on the stack, the operating points of the initial operation during EIS-measurements as well as the first and reference VI-curves are depicted in Fig. 9, together with chosen operating points during soaked start up.

As expected, due to the prolonged storage of the stack, the cell voltages during the initial operation are lowest, where 40.09 V were measured at 30 A after operation for more than 30 min. During the first VI-curve measurement, the cell voltages recover to 41.37 V at 30 A, showing the first recovery effects during operation and approaching the reference cell voltages of 43.17 V. This can be attributed to a multitude of factors [11,51], one of which is lacking humidification of the membranes, which is counteracted by operation and the temporal load reduction during VI-curve measurement.

After overnight – soaking, the membrane should be fully humidified and thus exhibit maximum proton conductivity. The immediate performance of the soaked stack upon start up was worse compared to the measurements before, due to severe flooding of the cathode compartment blocking the supply of oxygen to the cathode, however, once the blockages were removed, the stack did perform better, as evidenced by the last two data points of the curve in Fig. 9. In comparison to the initial and dry operation of the stack, a reduced membrane resistance was also measured even after it was operated under drying conditions through a low current of 3 A for over 35 min, as shown in Table 2.

The distribution and effect of the cathode and coolant channel flooding on the stack temperature is visualised in Fig. 10, which displays pictures taken with the IR-camera at different times during the start up. Fig. 10 a) - c) show the severe flooding and inhomogeneity in the temperature distribution during start up, which took more than 10 min. Likely, the flooding was blown out of the channels and the stack voltage properly recovered to levels above the previous operation. Fig. 10 d) shows beginning homogenisation of the temperature distribution across the stack, which preceded the stationary temperature distribution shown in Fig. 10 e). This can be seen as characteristic for prolonged operation of the stack at high currents.

4.2. Reconditioning by oxygen starvation

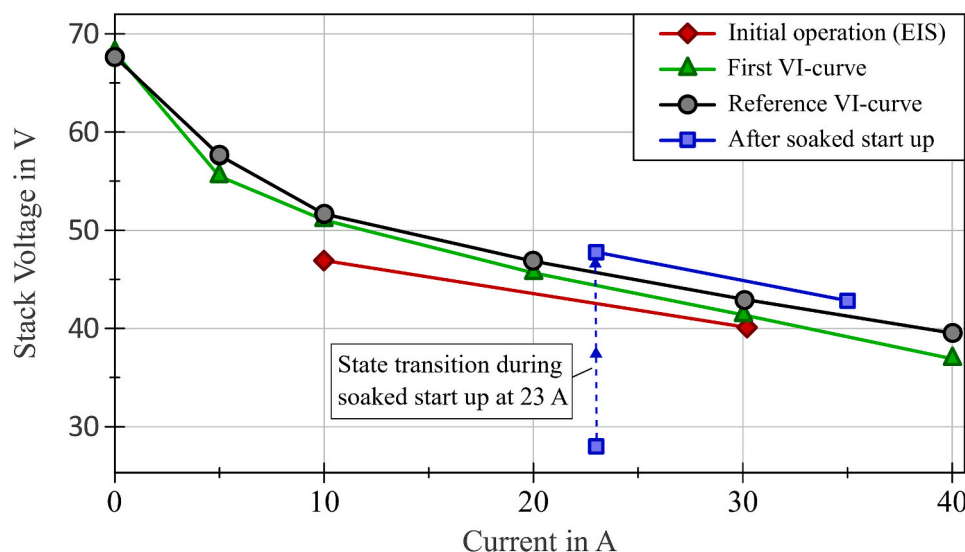The influence of the proposed reconditioning procedure according to

Fig. 9. VI-Curves of the stack for dry and pre-humidified operation.
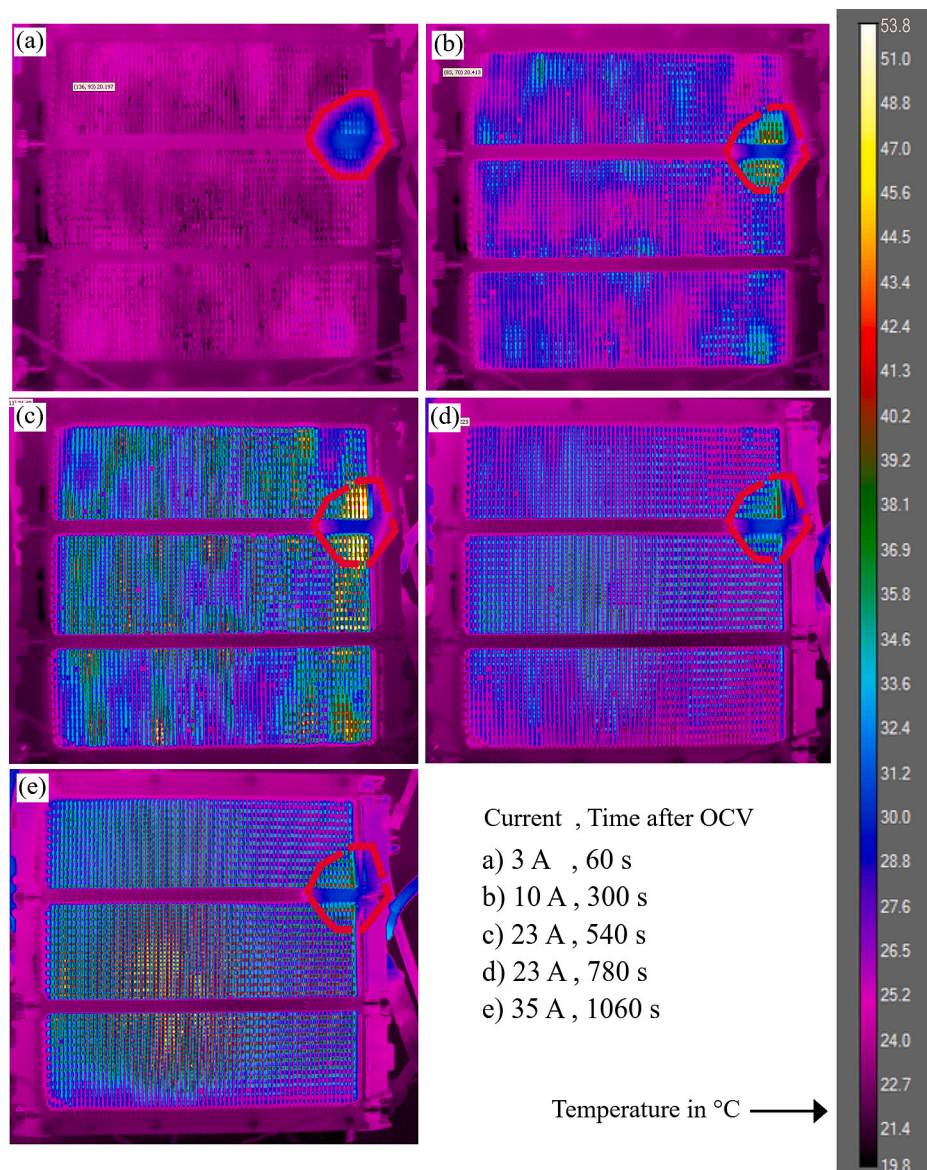
Fig. 10. IR-Pictures of the cathode inlet of the stack during system start up after overnight soaking (The red circled area is not to be evaluated, it corresponds to a defect of the IR-camera). (For interpretation of the references to colour in this figure legend, the reader is referred to the web version of this article.)

Section 2.3 can be seen in Fig. 11. The Figure shows the reference VI-curve as well as the corresponding stack voltages after the first and second reconditioning phases during load phase ramp-up shown in Fig. 3. Furthermore, Fig. 11 displays the measurement results from Fig. 4, which includes the average stack voltage of the EIS-measurement following the reconditioning procedure after the soaked start-up. Additionally, it illustrates the influence of the fourth reconditioning procedure at 35 A after the EIS-measurements.

The positive effect of the reconditioning procedure on the stack voltage is clearly visible and can be explained mainly by two reasons. The reduction of PtOx, which leads to a higher ECSA [11] and the production of water during the reconditioning phases without convective flow of air through the stack. By repeating the procedure, the stack voltage was further increased. This implies that conducting the procedure once is not yet sufficient to completely eliminate reversible degradation effects.

How lasting the effect of the reconditioning is, mainly depends on the average cell voltage of the stack as PtOx formation is forced in a voltage range of 0.60 V…0.95 V [65]. After soaked start up and a third reconditioning procedure, the stack was operated under low current operation

of 3 A for more than 35 min. During this time, the stack voltage decreased from 59.17 V to 56.70 V, corresponding to a decrease in average cell voltage from 822 mV to 788 mV (compare Fig. 4). It is assumed, that much of the effect from pre-humidifying and reconditioning is spoiled by the operation at low currents conditions, which are forcing membrane dry out and PtOx formation. This statement is supported by the increasing impedance during this operating point, as shown in Fig. 6 (b). However, a slight increase in stack voltage during the EIS-measurements from 10 A to 30 A can be seen.

After the EIS-measurements, a nearly constant stack voltage of 41.35 V was measured at a current of 35 A, whereby the voltage fluctuations due to anode purge are considered by building the average value of the last minute of the operational point. This is equivalent to an average cell voltage of 574 mV and corresponds to the reference point 1 after EIS-measurement in Fig. 11. Direct after the fourth reconditioning phase (point 2), a Stack voltage of 47.79 V was measured at 35 A, which decreases to 43.56 V after 10 min of operation (point 3). The mean stack voltage during this time equals 43.92 V, which resulted in approx. 6.2% more electrical energy provided by the stack at the same hydrogen consumption. Correspondingly less thermal energy is released from the
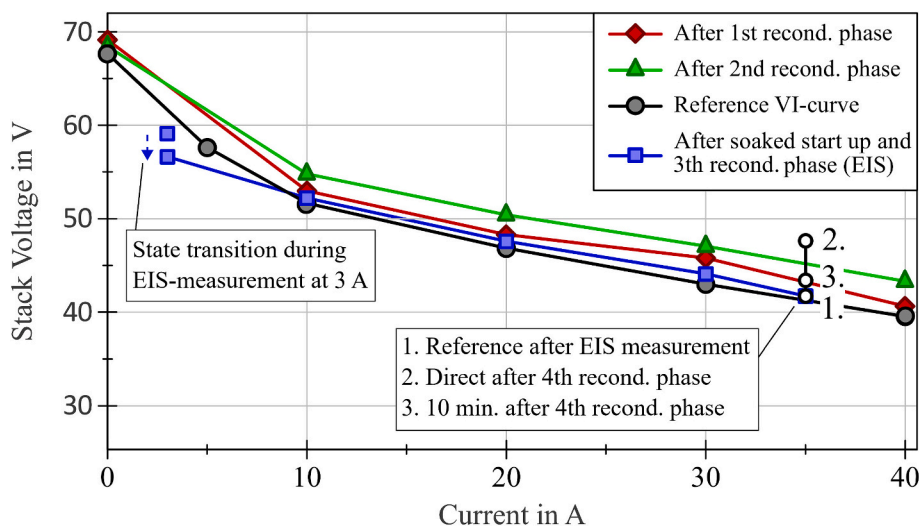
Fig. 11. VI-Curves of the stack before and after reconditioning by oxygen starvation.

stack, which helps to prevent the MEAs from drying out. It has to be mentioned, that extensive oxygen starvation will lead to degradation in form of inhomogeneous agglomeration of the platinum catalyst [66], whereas short-term starvation up to 100 s will not damage the cell according to [67].

4.3. Electrochemical impedance spectroscopy (EIS)

As visualised through the comparison of the relative residuals of the Kramers-Kronig analysis (Fig. 5 and Appendix A1, Figs. A1.1–5), the algorithm is able to extract the meaningful data from the noisy measurement. The data quality even after using the algorithm is still not ideal, as evidenced by the mismatch in the relative change of the membrane resistance before and after the overnight soaking between measurement and fitting. Especially in the high and low frequency regions a significant number of data points are eliminated by the algorithm, thereby showing, that especially for EIS measurements under non-stationary conditions, only a very limited frequency range (approximately 10 Hz - 15 kHz) can be investigated. However, the resulting data can be fitted using a common equivalent circuit structure for fuel cells (R-RQ-RQ in Voigt configuration) and does reflect the expected behaviour for the ohmic resistance (R_s) and the first of the parallel resistances (R_1). The resulting behaviour of R_2 at high current (30 A) is questionable. Closer inspection of the results in Table 1 show, that the change of this parameter from before the reconditioning to after it, is not equal in all three measurements. The value decreases in the first measurement, and increases in the other two. Since the value of R_2 very small the effect on the overall behaviour is negligible. It can be associated with the small, high frequency half circle in the Nyquist plot (Figs. A1.12–15 (b)), which is usually attributed to the anode reaction, which is not influenced by the oxygen starvation reconditioning procedure.

While one needs to be conscious of the limitations due to the poor quality of the original data and the limited frequency range, the fitting does produce reasonably accurate results for the most significant contributors in the fuel cells behaviour.

5. Conclusion and outlook

With increasing load current the voltage of the stack becomes increasingly fluctuating because the stack enters a vicious circle in terms of operation. As cooling and air supply to the cathode are driven by the same fan, an increase in the operating temperature, caused by a higher load current automatically leads to an increase of the fan speed in order

to control the temperature. Since the stack is already operating at a large λ-value, any increase of the airflow on the cathode side will dry out the stack even further, thus increasing the stack's impedance and thermal losses. This holds true for all open cathode stacks where cooling and cathode supply are not separately controllable. Furthermore, prolonged operation at low currents close to the OCV will cause the formation of PtOx, which will increase the stacks impedance and result in increased thermal losses, further advancing the vicious circle described above. Thus, a minimum current should be set even in idle operation to produce enough water and avoid OCV and correspondingly PtOx formation. Especially in systems powered by multiple stacks the operating strategy could fully shut down some of the stacks in low load situations, to keep the active stacks above the minimum current, even though this increases the overall system response time to a significant load step. Future EIS measurements at low load on open cathode stacks should employ a different procedure, because achieving a stable operating point and running through an entire EIS measurement proved to significantly change the characteristic of the stack (compare Sec. 4.2 and Fig. 4). In cases like this, the data acquisition procedure could be changed to allow for either less time to scan the required frequency range, scan multiple frequencies at once or realise the scan in multiple sections with controlled recovery periods in between, where the stack is operated at a higher current to re-humidify the stack before the membrane dries too much. Lastly, in order to improve the high frequency data, a corrective measurement of the setup with a known, very small resistance should be performed and subtracted from all subsequent measurements, to eliminate high frequency noise due to the cables and measurement setup. The proposed post-processing algorithm to improve the data quality for the model generation has been shown to improve the stationary accuracy of the model significantly. The next step will be to perform further experiments featuring characteristic load cycles and other highly dynamic processes and simulate the same load cycles with the fitted models.

Application of liquid water to the stack before start up caused severe flooding issues for the first 10 min of operation, inhibiting the performance. However, once the excess water had been expelled from the stack, the performance of the stack was better than the reference. To further address the PtOx issues, an oxygen starvation procedure of about 100 s in total duration was shown to improve the stacks performance. For 10 mins following the procedure the stack exhibited an improved efficiency under constant load providing 6.2% more el. energy at constant hydrogen consumption. Therefore, recovery procedures for stacks, which can be executed during system operation need to be investigated further.

CRediT authorship contribution statement

F. Becker: Writing – review & editing, Writing – original draft, Visualization, Methodology, Investigation, Formal analysis, Conceptualization. **C. Cosse:** Writing – review & editing, Writing – original draft, Investigation, Formal analysis, Conceptualization. **C. Gentner:** Writing – review & editing, Supervision, Funding acquisition. **D. Schulz:** Writing – review & editing, Supervision, Funding acquisition. **L. Liphardt:** Writing – review & editing, Methodology, Investigation, Conceptualization.

Declaration of competing interest

The authors declare that they have no known competing financial interests or personal relationships that could have appeared to influence the work reported in this paper.

Data availability

The authors do not have permission to share data.

Acknowledgements

Appendix A. Supplementary data

Supplementary data to this article can be found online at https://doi.org/10.1016/j.apenergy.2024.123048.

References

[1] Mench MM. Fuel Cell Engines. 1st ed. Wiley; 2008 [Online]. Available: https://onlinelibrary.wiley.com/doi/book/10.1002/9780470209769.

[2] Shahsavari S, Desouza A, Bahrami M, Kjeang E. Thermal analysis of air-cooled PEM fuel cells. 03603199 2012;37(23):18261–71. https://doi.org/10.1016/j.ijhydene.2012.09.075.

[3] Dicks A, Rand DAJ. Fuel cell systems explained. Hoboken, New Jersey: John Wiley & Sons Inc.; 2018.

[4] Atkinson RW, Hazard MW, Rodgers JA, Stroman RO, Gould BD. An open-cathode fuel cell for atmospheric flight. 0013–4651 2017;164(2):F46–54. https://doi.org/10.1149/2.0261702jes.

[5] Vetter R, Schumacher JO. Free open reference implementation of a two-phase PEM fuel cell model. 00104655 2019;234:223–34. https://doi.org/10.1016/j.cpc.2018.07.023.

[6] Cetinbas FC, Advani SG, Prasad AK. An improved agglomerate model for the pem catalyst layer with accurate effective surface area calculation based on the sphere-packing approach. 0013–4651 2014;161(6):F803–13. https://doi.org/10.1149/2.116406jes.

[7] Springer TE, Zawodzinski TA, Gottesfeld S. Polymer electrolyte fuel cell model. 0013–4651 1991;138(8):2334–42. https://doi.org/10.1149/1.2085971.

[8] Motupally S, Becker AJ, Weidner JW. Diffusion of water in nafion 115 membranes. 00134651 2000;147(9):3171. https://doi.org/10.1149/1.1393879.

[9] Mulyazmi WW, Daud S Octavia, Ulfah M. The relative humidity effect of the reactants flows into the cell to increase PEM fuel cell performance. MATEC Web Conf 2018;156:3033. https://doi.org/10.1051/matecconf/201815603033.

[10] Zhang J, Wang C, Zhang A. Experimental study on temperature and performance of an open-cathode PEMFC stack under thermal radiation environment. Appl Energy 2022;311:118646. https://doi.org/10.1016/j.apenergy.2022.118646.

[11] Mitzel J, Zhang Q, Gazdzicki P, Friedrich KA. Review on mechanisms and recovery procedures for reversible performance losses in polymer electrolyte membrane fuel cells. 03787753 2021;488:229375. https://doi.org/10.1016/j.jpowsour.2020.229375.

[12] Berning T, Djilali N. Three-dimensional computational analysis of transport phenomena in a PEM fuel cell—a parametric study. *03787753* 2003;124(2):440–52. https://doi.org/10.1016/S0378-7753(03)00816-4.

[13] Wang L. A parametric study of PEM fuel cell performances. *03603199* 2003;28(11):1263–72. https://doi.org/10.1016/S0360-3199(02)00284-7.

[14] Gasteiger HA, Panels JE, Yan SG. Dependence of PEM fuel cell performance on catalyst loading. 03787753 2004;127(1–2):162–71. https://doi.org/10.1016/j.jpowsour.2003.09.013.

[15] Pathapati PR, Xue X, Tang J. A new dynamic model for predicting transient phenomena in a PEM fuel cell system. 09601481 2005;30(1):1–22. https://doi.org/10.1016/j.renene.2004.05.001.

[16] Ferng Y. Analytical and experimental investigations of a proton exchange membrane fuel cell. *03603199* 2004;29(4):381–91. https://doi.org/10.1016/S0360-3199(03)00159-9.

[17] Schwarz DH, Djilali N. 3D modeling of catalyst layers in PEM fuel cells. 00134651 2007;154(11):B1167. https://doi.org/10.1149/1.2777011.

[18] Inoue G, Yoshimoto T, Matsukuma Y, Minemoto M, Itoh H, Tsurumaki S. Effect of flow pattern of gas and cooling water on relative humidity distribution in polymer electrolyte fuel cell. *03787753* 2006;162(1):94–104. https://doi.org/10.1016/j.jpowsour.2006.07.018.

[19] Inoue G, Yoshimoto T, Matsukuma Y, Minemoto M, Itoh H, Tsurumaki S. Numerical analysis of relative humidity distribution in polymer electrolyte fuel cell stack including cooling water. *03787753* 2006;162(1):81–93. https://doi.org/10.1016/j.jpowsour.2006.07.017.

[20] Huisseune H, Willockx A, Depaepe M. Semi-empirical along-the-channel model for a proton exchange membrane fuel cell. *03603199* 2008;33(21):6270–80. https://doi.org/10.1016/j.ijhydene.2008.08.013.

[21] Scholta J, Häussler F, Zhang W, Küppers L, Jörissen L, Lehnert W. Development of a stack having an optimized flow field structure with low cross transport effects. *03787753* 2006;155(1):60–5. https://doi.org/10.1016/j.jpowsour.2005.05.101.

[22] Chang PA, St-Pierre J, Stumper J, Wetton B. Flow distribution in proton exchange membrane fuel cell stacks. 03787753 2006;162(1):340–55. https://doi.org/10.1016/j.jpowsour.2006.06.081.

[23] Liu Z, Mao Z, Wang C, Zhuge W, Zhang Y. Numerical simulation of a mini PEMFC stack. *03787753* 2006;160(2):1111–21. https://doi.org/10.1016/j.jpowsour.2006.03.001.

[24] Sagar A, Chugh S, Sonkar K, Sharma A, Kjeang E. A computational analysis on the operational behaviour of open-cathode polymer electrolyte membrane fuel cells. *03603199* 2020;45(58):34125–38. https://doi.org/10.1016/j.ijhydene.2020.09.133.

[25] Sasmito AP, Lum KW, Birgersson E, Mujumdar AS. Computational study of forced air-convection in open-cathode polymer electrolyte fuel cell stacks. 03787753 2010;195(17):5550–63. https://doi.org/10.1016/j.jpowsour.2010.02.083.

[26] Dutta SSS. Numerical prediction of temperature distribution in PEM fuel cells. 1040–7782 2000;38(2):111–28. https://doi.org/10.1080/10407780050135360.

[27] Fuller TF, Newman J. Water and thermal management in solid-polymer-electrolyte fuel cells. 0013–4651 1993;140(5):1218–25. https://doi.org/10.1149/1.2220960.

[28] Ju H, Meng H, Wang C-Y. A single-phase, non-isothermal model for PEM fuel cells. Int J Heat Mass Transf 2005;48(7):1303–15. https://doi.org/10.1016/j.ijheatmasstransfer.2004.10.004.

[29] Chupin S, et al. Numerical investigation of the impact of gas and cooling flow configurations on current and water distributions in a polymer membrane fuel cell through a pseudo-two-dimensional diphasic model. *03787753* 2010;195(16):5213–27. https://doi.org/10.1016/j.jpowsour.2010.03.027.

[30] Promislow K, Wetton B. A simple, mathematical model of thermal coupling in fuel cell stacks. *03787753* 2005;150:129–35. https://doi.org/10.1016/j.jpowsour.2005.02.032.

[31] Shan Y, Choe S-Y. A high dynamic PEM fuel cell model with temperature effects. *03787753* 2005;145(1):30–9. https://doi.org/10.1016/j.jpowsour.2004.12.033.

[32] Yu S, Jung D. Thermal management strategy for a proton exchange membrane fuel cell system with a large active cell area. *09601481* 2008;33(12):2540–8. https://doi.org/10.1016/j.renene.2008.02.015.

[33] Pharoah JG, Burheim OS. On the temperature distribution in polymer electrolyte fuel cells. 03787753 2010;195(16):5235–45. https://doi.org/10.1016/j.jpowsour.2010.03.024.

[34] Adzakpa KP, et al. Transient air cooling thermal modeling of a PEM fuel cell. 03787753 2008;179(1):164–76. https://doi.org/10.1016/j.jpowsour.2007.12.102.

[35] Sinha PK, Wang C-Y, Beuscher U. Transport phenomena in elevated temperature PEM fuel cells. 00134651 2007;154(1):B106. https://doi.org/10.1149/1.2393014.

[36] Andisheh-Tadbir M, Desouza A, Bahrami M, Kjeang E. Cell level modeling of the hygrothermal characteristics of open cathode polymer electrolyte membrane fuel cells. *03603199* 2014;39(27):14993–5004. https://doi.org/10.1016/j.ijhydene.2014.07.049.

[37] Andisheh Tadbir M, Shahsavari S, Bahrami M, Kjeang E. Thermal management of an air-cooled PEM fuel cell: Cell level simulation. 2012. p. 453–9. https://doi.org/10.1115/fuelcell2012-91440.

[38] Yang Y, et al. Overall and local effects of operating parameters on water management and performance of open-cathode PEM fuel cells. *03062619* 2022;315:118978. https://doi.org/10.1016/j.apenergy.2022.118978.

[39] Mahjoubi C, Olivier J-C, Skander-mustapha S, Machmoum M, Slama-belkhodja I. An improved thermal control of open cathode proton exchange membrane fuel cell. *03603199* 2019;44(22):11332–45. https://doi.org/10.1016/j.ijhydene.2018.11.055.

[40] Ondrejička K, Ferencey V, Stromko M. Modeling of the air-cooled PEM fuel cell. *24058963* 2019;52(27):98–105. https://doi.org/10.1016/j.ifacol.2019.12.740.

[41] Yu X, Liu Y, Tu Z, Chan SH. Endplate effect in an open-cathode proton exchange membrane fuel cell stack: Phenomenon and resolution. 09601481 2023;219:119392. https://doi.org/10.1016/j.renene.2023.119392.

[42] Yu X, Cai S, Luo X, Tu Z. Barrel effect in an air-cooled proton exchange membrane fuel cell stack. Energy 2024;286:129668. https://doi.org/10.1016/j.energy.2023.129668.

[43] Xing S, et al. Recent advances in heat and water management of forced-convection open-cathode proton exchange membrane fuel cells. Renew Sustain Energy Rev 2022;165:112558. https://doi.org/10.1016/j.rser.2022.112558.

[44] Kurnia JC, Chaedir BA, Sasmito AP, Shamim T. Progress on open cathode proton exchange membrane fuel cell: Performance, designs, challenges and future

directions. 03062619 2021;283:116359. https://doi.org/10.1016/j.apenergy.2020.116359.

[45] Al-Zeyoudi H, Sasmito AP, Shamim T. Performance evaluation of an open-cathode PEM fuel cell stack under ambient conditions: case study of United Arab Emirates. Energ Conver Manage 2015;105:798–809. https://doi.org/10.1016/j.enconman.2015.07.082.

[46] Wang Z, Tongsh C, Wang B, Liu Z, Du Q, Jiao K. Operation characteristics of open-cathode proton exchange membrane fuel cell with different cathode flow fields. Sustain Energy Technol Assess 2022;49:101681. https://doi.org/10.1016/j.seta.2021.101681.

[47] Shen J, Du C, Yan F, Chen B, Tu Z. Experimental study on the dynamic performance of a power system with dual air-cooled PEMFC stacks. *03062619* 2022;326:120025. https://doi.org/10.1016/j.apenergy.2022.120025.

[48] Le P-L, Devi N, Chou J, Arpornwichanop A, Chen Y-S. A novel design for humidifying an open-cathode proton exchange membrane fuel cell using anode purge. Int J Hydrogen Energy 2022;47(64):27680–9. https://doi.org/10.1016/j.ijhydene.2022.06.087.

[49] Fan L, Liu Y, Luo X, Tu Z, Chan SH. A novel gas supply configuration for hydrogen utilization improvement in a multi-stack air-cooling PEMFC system with dead-ended anode. Energy 2023;282:129004. https://doi.org/10.1016/j.energy.2023.129004.

[50] U.S. Department of Energy, Technical Report. 2016.

[51] Gazdzicki P, Mitzel J, Garcia Sanchez D, Schulze M, Friedrich KA. Evaluation of reversible and irreversible degradation rates of polymer electrolyte membrane fuel cells tested in automotive conditions. 03787753 2016;327:86–95. https://doi.org/10.1016/j.jpowsour.2016.07.049.

[52] Tsotridis G, Pilenga A, de Marco G, Malkow T. EU harmonised test protocols for PEMFC MEA testing in single cell configuration for automotive applications. 2015.

[53] Zago M, et al. Experimental analysis of recoverable performance loss induced by platinum oxide formation at the polymer electrolyte membrane fuel cell cathode. *0378-7753* 2020;455:227990. https://doi.org/10.1016/j.jpowsour.2020.227990.

[54] Darling RM, Meyers JP. Kinetic model of platinum dissolution in PEMFCs. 00134651 2003;150(11):A1523. https://doi.org/10.1149/1.1613669.

[55] Xu H, Kunz R, Fenton JM. Investigation of platinum oxidation in pem fuel cells at various relative humidities. 10990062 2007;10(1):B1. https://doi.org/10.1149/1.2372230.

[56] Lin L-C, Cheng Y-S, Liao W-C, Huang Y-H, Pan Y-T. Transient loss and recovery of platinum fuel cell cathode catalyst at high voltage efficiency regimes. *00134651* 2021;168(5):54503. https://doi.org/10.1149/1945-7111/abf974.

[57] Balogun E, Barnett AO, Holdcroft S. Cathode starvation as an accelerated conditioning procedure for perfluorosulfonic acid ionomer fuel cells. J Power Sour Adv 2020;3:100012. https://doi.org/10.1016/j.powera.2020.100012.

[58] Intelligent Energy. AC64DS0117DH: AC64-Datasheet. 2017.

[59] Sabawa JP, Bandarenka AS. Applicability of double layer capacitance measurements to monitor local temperature changes at polymer electrolyte membrane fuel cell cathodes. Res Chem 2020;2:100078. https://doi.org/10.1016/j.rechem.2020.100078.

[60] Ivan Pivac FB. Rejuvenation techniques for automotive fuel cells: Giantleap improves automation of non-polluting transportation with lifetime extension of automotive PEM fuel cells. 2019.

[61] Latorrata S, Pelosato R, Gallo Stampino P, Cristiani C, Dotelli G. Use of electrochemical impedance spectroscopy for the evaluation of performance of PEM fuel cells based on carbon cloth gas diffusion electrodes. J Spectrosc 2018;2018:1–13. https://doi.org/10.1155/2018/3254375.

[62] Boukamp BA. A linear Kronig-Kramers transform test for immittance data validation. 0013–4651 1995;142(6):1885–94. https://doi.org/10.1149/1.2044210.

[63] Schönleber M, Klotz D, Ivers-Tiffée E. A method for improving the robustness of linear Kramers-Kronig validity tests. *00134686* 2014;131:20–7. https://doi.org/10.1016/j.electacta.2014.01.034.

[64] Knudsen Kristian. *kbknudsen/PyEIS: PyEIS: A Python-based Electrochemical Impedance Spectroscopy simulator and analyzer*: Zenodo. 2019. Accessed: Oct. 27 2023. [Online]. Available: https://zenodo.org/records/2535951.

[65] Basha ABM, Karan K. Understanding potential decay during OCV hold via dry recovery process. J Electrochem Soc 2023;170(6):64505. https://doi.org/10.1149/1945-7111/acd724.

[66] Bodner M, Schenk A, Salaberger D, Rami M, Hochenauer C, Hacker V. Air starvation induced degradation in polymer electrolyte fuel cells. Fuel Cells 2017;17(1):18–26. https://doi.org/10.1002/fuce.201600132.

[67] Su H, Ye D, Cai Y, Guo W. Air starvation of proton exchange membrane fuel cells and its beneficial effects on performance. *03062619* 2022;323:119626. https://doi.org/10.1016/j.apenergy.2022.119626.